The chemical dynamics of nanosensors capable of single-molecule detection

Ardemis A. Boghossian, Jingqing Zhang, François T. Le Floch-Yin, Zachary W. Ulissi, Peter Bojo et al.

Citation: J. Chem. Phys. **135**, 084124 (2011); doi: 10.1063/1.3606496
View online: http://dx.doi.org/10.1063/1.3606496
View Table of Contents: http://jcp.aip.org/resource/1/JCPSA6/v135/i8
Published by the American Institute of Physics.

The chemical dynamics of nanosensors capable of single-molecule detection

Ardemis A. Boghossian,[1,a)] Jingqing Zhang,[1,a)] François T. Le Floch-Yin,[2] Zachary W. Ulissi,[1] Peter Bojo,[3] Jae-Hee Han,[4] Jong-Ho Kim,[5] Jyoti R. Arkalgud,[1] Nigel F. Reuel,[1] Richard D. Braatz,[1] and Michael S. Strano[1,b)]

[1]*Department of Chemical Engineering, Massachusetts Institute of Technology, Cambridge, Massachusetts 02139, USA*
[2]*Department of Aeronautics and Astronautics, Massachusetts Institute of Technology, Cambridge, Massachusetts 02139, USA*
[3]*Department of Biological Engineering, Massachusetts Institute of Technology, Cambridge, Massachusetts 02139, USA*
[4]*Department of Energy IT, Kyungwon University, Seongnam, Gyeonggi-do 461-701, South Korea*
[5]*Department of Chemical Engineering, Hanyang University, Ansan 426-791, Republic of Korea*

(Received 14 April 2011; accepted 12 June 2011; published online 31 August 2011)

Recent advances in nanotechnology have produced the first sensor transducers capable of resolving the adsorption and desorption of single molecules. Examples include near infrared fluorescent single-walled carbon nanotubes that report single-molecule binding via stochastic quenching. A central question for the theory of such sensors is how to analyze stochastic adsorption events and extract the local concentration or flux of the analyte near the sensor. In this work, we compare algorithms of varying complexity for accomplishing this by first constructing a kinetic Monte Carlo model of molecular binding and unbinding to the sensor substrate and simulating the dynamics over wide ranges of forward and reverse rate constants. Methods involving single-site probability calculations, first and second moment analysis, and birth-and-death population modeling are compared for their accuracy in reconstructing model parameters in the presence and absence of noise over a large dynamic range. Overall, birth-and-death population modeling was the most robust in recovering the forward rate constants, with the first and second order moment analysis very efficient when the forward rate is large ($>10^{-3}$ s^{-1}). The precision decreases with increasing noise, which we show masks the existence of underlying states. Precision is also diminished with very large forward rate constants, since the sensor surface quickly and persistently saturates. © *2011 American Institute of Physics*. [doi:10.1063/1.3606496]

I. INTRODUCTION

Recent advances in the fluorescence detection of individual molecules have motivated interest in single-molecule dynamics and analytical methods for understanding their networks of transitions.[1–14] Traditionally, these measurements have provided scientists with insight into previously intractable phenomena, ranging from enzyme and protein[2,15–24] conformational dynamics to various inner cell mechanisms.[25–32] These measurements have elucidated the mechanisms behind conformationally heterogeneous systems that would otherwise remain ambiguous using conventional bulk measurements susceptible to ensemble averaging. Current advancements in the field have extended the application of single-molecule measurements to the development of nanotube-based sensors capable of resolving single-molecule adsorption dynamics.[33–37]

In these particular systems, adsorption or binding of a specific molecule onto a single-walled carbon nanotube (SWCNT) results in the step-wise quenching of the nanotube fluorescence (Figure 1(a)). Each single adsorption event of a quenching molecule onto an unquenched segment of the nanotube results in a discrete decrease in SWCNT fluorescence intensity. Although these quenching events are indicative of the presence or absence of the molecule of interest, a more quantitative analysis is required to determine properties such as analyte concentration or flux. Specifically, these quenching events can be modeled as a series of reversible adsorption reactions on the SWCNT with a forward rate constant of k_f and a reverse rate constant of k_r (Figure 1(b)). As we have shown previously,[37] these reactions obey rate laws of orders greater than 0, and an increase in analyte concentration results in an increase in the forward rate. Recent studies have focused on using a variety of techniques for extracting rate information from single-molecule fluorescence events, including variations of hidden Markov modeling[33,37–45] and information theory.[46,47]

In this study, we exploit the parallelism of these different methods for extracting rate information and compare their accuracies under various kinetic conditions in the presence of simulated noise. A summary of this comparative analysis is shown in Figure 2. Simulated traces, much like the one shown in Figure 1(a), are generated under various forward rate, re-

a)These authors contributed equally to this work.
b)Author to whom correspondence should be addressed. Electronic mail: strano@mit.edu.

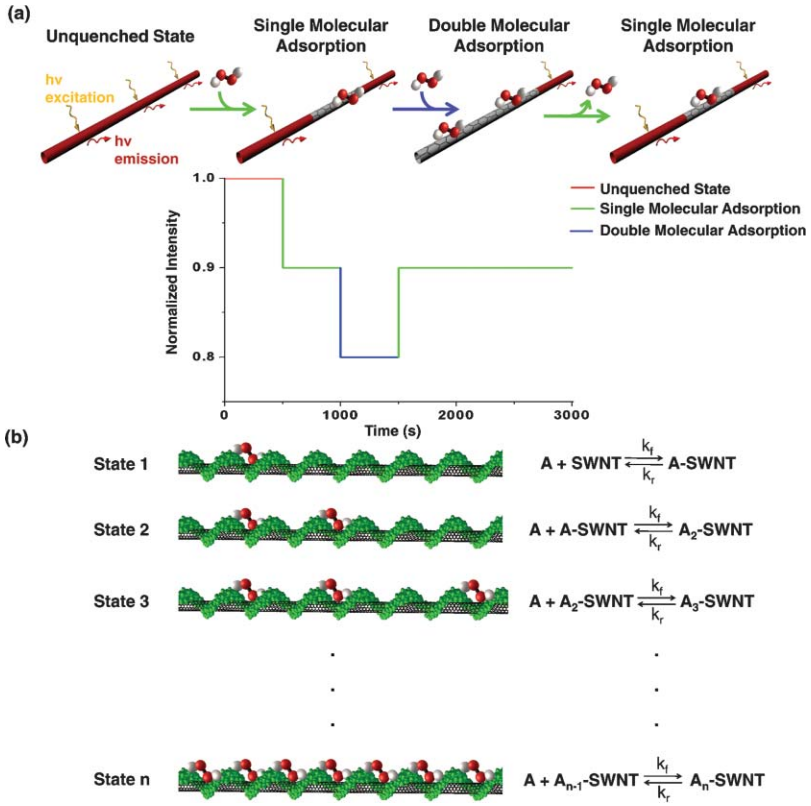

FIG. 1. Single-molecule fluorescence quenching events. (a) Sample intensity trace of a SWCNT undergoing subsequent analyte adsorption and desorption events demonstrates changes in intensity. Single-molecule adsorption events result in the stepwise decrease in fluorescence whereas desorption events result in the stepwise increase in fluorescence. (b) Adsorption and desorption reactions can be modeled as a series of reversible adsorption reaction steps. The forward rate constant, k_f, and the reverse rate constant, k_r, determine the rate of adsorption and desorption, respectively.

verse rate, and noise conditions. In the first step of the analysis, we determine the total number of states, or fluorescence intensity levels, the sensor exhibits in each trace. In the second step of the analysis, we use this information to fit the simulated trace to an idealized, de-noised trace, as would be done to traces obtained experimentally. Using these fitted traces, we calculate the extracted forward and reverse reaction rate constants in the third step of the analysis and compare them to the input values to compute an error. Each of these steps is described in detail below.

II. GENERATING SIMULATED TRACES

In order to simulate experimental SWCNT fluorescence traces in the presence of different concentrations of analyte, a kinetic Monte Carlo (KMC) algorithm was implemented.[48]

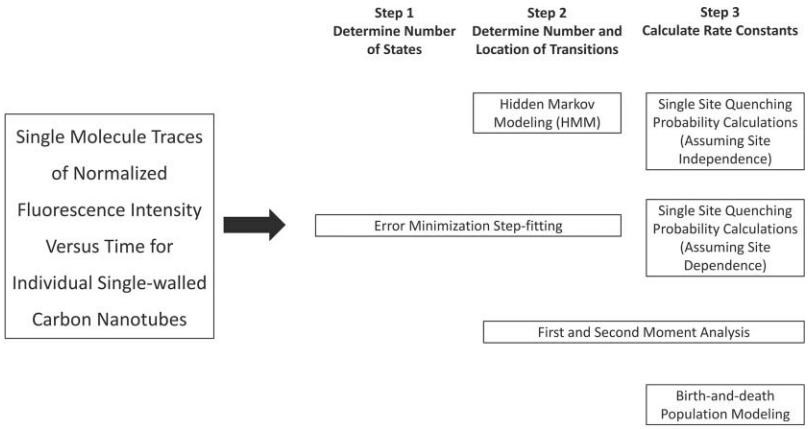

FIG. 2. Outline of algorithms used for rate calculations. Different algorithms can be used for calculating and comparing the concentration-dependent rate constants. Fluorescence traces are analyzed to determine rate constants using three steps. In the first step, the algorithm determines the number of states that are expressed by the trace. The maximum number of states expressed by the trace is then used in the second step of the algorithm where the trace is fit to an idealized trace specifying the number and location of the transitions. In the third step of the algorithm, the frequency of these transitions is used to calculate corresponding forward and reverse rate constants.

In a detailed study performed by Harrah and Swan,[49] the stochastic fluctuation of nanotube fluorescence was examined under exciton diffusion-limiting conditions. Introduction and removal of dynamic point defects were distributed throughout the nanotube length to obtain time- and spatially resolved quantum efficiencies of a fluorescing nanotube. To simulate the diffraction-limited experimental conditions, overall nanotube florescence emissions were determined from concentration-based binding rates. For a specified pair of forward and reverse rate constants, reaction probabilities for adsorption and desorption during the next reaction event were determined from the product of the forward rate and reverse rate constants, respectively, with the maximum number of sites per nanotube. The expressions below differ from standard chemical kinetics in two important ways: (1) the concentration of ligand is assumed to be constant and lumped into the forward rate constant, and (2) since the calculation looks at a single nanotube, the number of sites, and not a nanotube concentration, is appropriate.

Based on these guidelines, reaction events are assumed to occur with probabilities, P_{rxn}, according to a Poisson process,[50,51]

$$P_{rxn} = e^{-(k_f Q_{empty} + k_r Q_{occupied})t}, \tag{1}$$

where k_f is the forward reaction rate constant, Q_{empty} is the number of empty sites on the nanotube, k_r is the reverse rate constant, $Q_{occupied}$ is the number of occupied sites, and t is the time. At each reaction event, either an adsorption or desorption instance takes. The probability of an adsorption event occurring in the forward reaction becomes

$$P_f = \frac{k_f Q_{empty}}{k_f Q_{empty} + k_r Q_{occupied}}. \tag{2}$$

Subsequently, the probability of the reverse reaction occurring becomes

$$P_r = 1 - P_f. \tag{3}$$

For SWCNTs with an average length of ~900 nm, a recent experimental estimate of the exciton excursion distance[37] resulted in ~90 nm, so we expected no more than $Q_{total} = 10$ states typically. We impose a site balance as

$$Q_{empty} + Q_{occupied} = Q_{total}. \tag{4}$$

As discussed above, the forward reaction results in a step decrease in fluorescence whereas the reverse reaction results in a step increase. These reaction events were carried out for a total reaction time of 3000 s to simulate observation times used experimentally.[35,37] This simulation was repeated to generate 100 SWCNT fluorescence traces at each specified forward rate constant, reverse rate constant, and noise level. Forward rate constants were varied over 7 orders of magnitude, ranging from 10^{-5}–10 s^{-1}, and reverse rate constants were varied over 8 orders of magnitude, ranging from 10^{-10}–10^{-3} s^{-1}.

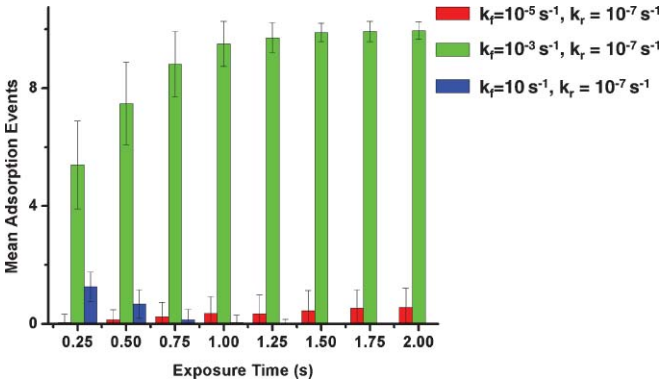

FIG. 3. Effect of exposure on perceived adsorption and desorption events. The number of adsorption events with varying forward rates and exposure times were counted and averaged over 100 traces. At high adsorption rates, the number of perceived binding instances increases with decreasing exposure times.

A. Effect of observation or exposure time

To simulate data collected experimentally, reaction events were binned in time assuming a finite observation time, similar to an exposure or shutter time from a camera or light collection device. This binning is required in practice and does result in the loss of adsorption and desorption events. The KMC was written to account for the net adsorption at each exposure interval. We examined the effect of exposure time on the accuracy of the analysis, specifically with respect to varying rates (Figure 3). As shown in the figure, at relatively high adsorption rates, the number of observed binding events increases with decreasing exposure times. With decreasing exposure times, the number of observed transitions approaches the number of actual transitions. Therefore, smaller exposure times are expected to yield a more accurate count of adsorption events. To simulate typical experimental conditions, an exposure time of 1 s was used throughout the course of this study.

The variance in the KMC model due to stochastic effects can be solved exactly.[52] For fixed forward and backward rate constants k_f and k_r, the stochastic relative standard deviation will scale with $1/\sqrt{Q_{\text{total}}}$. Thus, as the number of sites becomes large, the KMC model will converge to the continuum solution. This is intuitive, as the nanotube sites are considered to be independent in the KMC code. Observing increasing numbers of independent stochastic elements should decrease the observed stochastic variance with independent variations averaging out.

As shown in Figure 4, these ranges in rate constants have captured the wide variety of traces possible under experimental conditions. Reactions where $k_r \gg k_f$ result in traces with very few quenching steps, which are almost immediately recovered due to the relatively high reverse rate. Reactions where $k_f \gg k_r$, on the other hand, result in the immediate, complete quenching of the nanotube florescence. In cases where both k_f and k_r are large, we observe multiple instances of quenching and dequenching steps, whereas in cases where both constants are low, we observe almost no quenching/dequenching events. Traces with intermediate values, with k_f

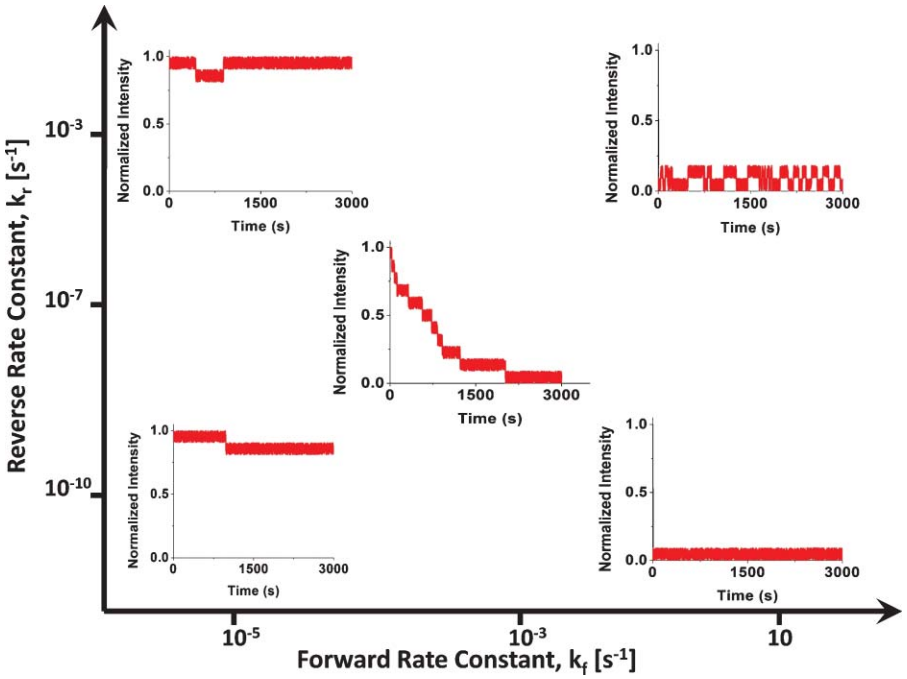

FIG. 4. Variety of traces generated from the KMC simulation. Various values of k_f and k_r were used to generate traces, with sample traces shown. Intensity traces were generated for randomized KMC quenching and unquenching events, where the probability of adsorption and desorption are governed by the magnitude of the forward and reverse rate constants, respectively. Forward rate constants were varied over 7 orders of magnitude whereas reverse rate constants were varied over 8 orders. Traces with large equilibrium constants ($k_f \gg k_r$) exhibit complete quenching within the first few frames, and traces with small equilibrium constants ($k_f \ll k_r$) exhibit immediate instances of desorption. Representative traces from previous studies[35,37] are centered within the range of forward and reverse rate constants tested, with $k_f \sim 10^{-3}$ s^{-1}, $k_r \sim 10^{-7}$ s^{-1}.

$\sim 10^{-3}$ and $k_r \sim 10^{-7}$, shown at the center of the figure, are representative of typical traces observed under most common experimental conditions.[35,37]

Traces were also generated under 5 different noise levels for each combination of k_f and k_r. At each timestep, a random value between -0.5 and 0.5 is added to the fluorescence intensity. To simulate different noise levels, this random number is multiplied by a noise scaling factor. In this study, we examined scaling factors with values of 0 (no noise), 0.05, 0.10, 0.20, and 0.40 with corresponding root mean squares (rms) of 0, 0.22, 0.32, 0.45, and 0.63, in units of normalized intensity (I/I_o).

III. STEP 1: DETERMINING THE NUMBER OF STATES

Once the simulated traces were generated, the first step of the analysis is determining the number of states, or fluorescence levels, demonstrated by each trace. To do this, we implemented an error-minimizing stepping algorithm.[53] In this algorithm, we initially fit the simulated trace to a flat trace with a value equal to the mean value of the simulated trace, or

$$I_{fit}(t) = \frac{\sum_{n=0}^{n=\frac{t_{final}}{\Delta t}} I_{\exp}(t = n\Delta t)}{\frac{t_{final}}{\Delta t} + 1}, \tag{5}$$

where I_{fit} is the best-fit intensity value as a function of time, t, I_{exp} is the experimental intensity value at time t, Δt is the exposure time, t_{final} is the final time of the trace (which is a multiple of the exposure time), and n is an integer ranging from 0 to $t_{final}/\Delta t$. We then assume the existence of a step and iteratively specify the location of this step at each time value in the trace. At each iteration, the error between the fitted trace and the simulated trace is calculated and compared to the initial error between the simulated trace and the flat trace that contains no quenching steps. If the addition of a step results in a better fit than the initial flat trace, then that trace is selected as the best fit. Thus, best fits are achieved by minimizing the mean-square error, ε,

$$\varepsilon = \sum_{n=0}^{n=\frac{t_{final}}{\Delta t}} |I_{fit}(t = n\Delta t) - I_{\exp}(t = n\Delta t)|. \tag{6}$$

The location of the step is determined by the trace that exhibits the least amount of error. Once the error-minimized location of the first step is determined, we assume the existence of an additional step on either side of the first step and once more evaluate the existence and location of steps. The process is repeated until it is determined that no more steps appear in the trace. In summary, this technique performs an iterative, error-minimization fitting analogous to that of linear regression (Figure 5). Once the traces have been fit using this error-minimized, step-fitting algorithm, the total number of states is determined by counting the number of different florescence levels each best-fit trace exhibits.

IV. STEP 2: DETERMINING THE NUMBER AND LOCATION OF TRANSITIONS

The number of states determined for each trace is next used to fit the simulated traces to idealized, de-noised traces

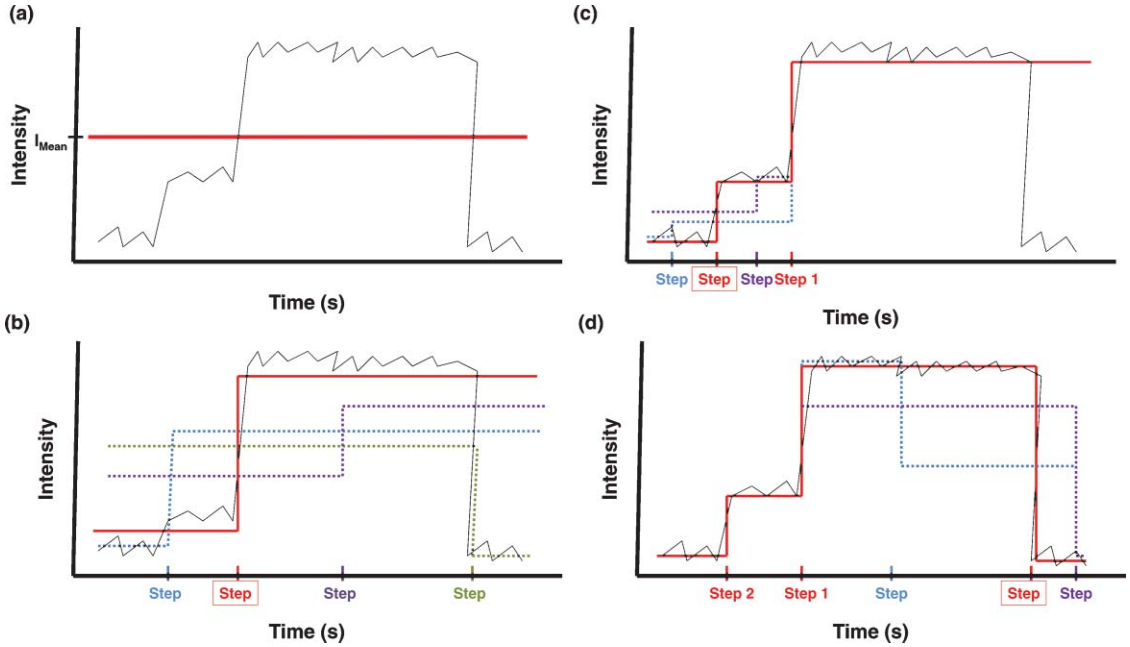

FIG. 5. Error-minimizing algorithm for fitting traces. Experimental traces were fit using a sequential, error-minimizing stepping algorithm. (a) Initially, the best-fit trace is obtained assuming a uniform value equal to the mean value of the trace. (b) Steps are sequentially assumed at each time frame, where the intensity value before the step is the mean intensity value before the transition, and the intensity value after the step is the mean intensity value after the transition. Sample traces are shown in blue, red, purple, and green. These fits are compared to the initial fit obtained in (a), and the traces demonstrating the least error (red) is selected as the best-fit trace. (c) After the location and size of the first step is obtained, the process is repeated for the portion of the trace prior to the transition. Sample traces are shown in blue, red, and purple. As before, these traces are compared to the fit obtained in (b), and the trace demonstrating the least error (red) is selected. (d) The process is also repeated for the portion of the trace after the transition, where steps are sequentially assumed to occur at each time frame. Sample traces are shown in blue, red, and purple, and the best-fit trace (red) is selected. For each of the new steps described in (c) and (d), the algorithm is repeated for the portions before and after each step until a globally minimized best-fit is obtained.

using three fitting algorithms: error-minimized step fitting, hidden Markov modeling, and first and second moment analysis. When determining the number of states using the error-minimized, step-fitting algorithm described above, the simulated trace is essentially already fit to an idealized trace contained quenching and de-quenching steps. Hence, this algorithm can be used to directly fit the simulated traces to idealized, best-fit traces.

The second method for fitting the simulated traces is hidden Markov modeling.[54] As described in earlier work,[33,37–45] steps are fit to the simulated traces in a manner that maximizes probability of the stochastic quenching and dequenching events.

The third method used to fit simulated traces is a moment analysis. A system of first order reactions can be shown to have a first moment (mean) that is equivalent to the continuum solution, even when populations are discrete and the system behaves stochastically (jumping between states).[55] The continuous model for this reaction is

$$A_0 + \theta_0 \underset{k_r}{\overset{k_f}{\rightleftarrows}} A\theta,$$

where A_0 is the free analyte molecule, θ_0 is a free binding site on the SWCNT, and $A\theta$ is the molecule bound to the SWCNT site with a binding rate constant of k_f and a reverse rate constant k_r. Assuming mass action kinetics, the rate of change for the concentration of the bound sites $[A\theta]$ is related to the concentrations of the free analyte $[A_0]$ and free sites $[\theta_0]$ according to the relation

$$\frac{d[A\theta]}{dt} = k_f[A_0][\theta_0] - k_r[A\theta]. \tag{7}$$

Furthermore, the three species will be related through a site balance

$$[\theta_0] + [A\theta] = [\theta_T], \tag{8}$$

where $[\theta_T]$ is the overall site concentration. Assuming the fluorescence intensity is related linearly to the concentration of empty sites and normalized by the intensity at $t = 0$, the mean intensity (the first moment) for an initially empty surface ($[A\theta] = 0$, $[\theta_0] = [\theta_T]$) will be

$$\langle I\rangle(t) = \frac{k_r + k_f e^{-(k_f+k_r)(t-t_0)}}{k_f + k_r}. \tag{9}$$

The mean normalized intensity $\langle I\rangle(t)$ will be unity at $t = 0$ and tend to the equilibrium value $k_r/(k_f + k_r)$ at long times.

Two primary effects will cause the observed intensity signal to deviate from this first moment: fluctuations from the stochastic nature of the process and measurement noise in the fluorescence signal. Modeling the time-dependent stochastic variance in the signal requires a discrete model, such as the birth-and-death model presented later. The stochastic variance will scale with $1/\sqrt{\theta_T}$ as discussed above. For large numbers of sites, the larger effect will be measurement error in the fluorescence signal. Including an error model can improve the fitting procedure. The error was

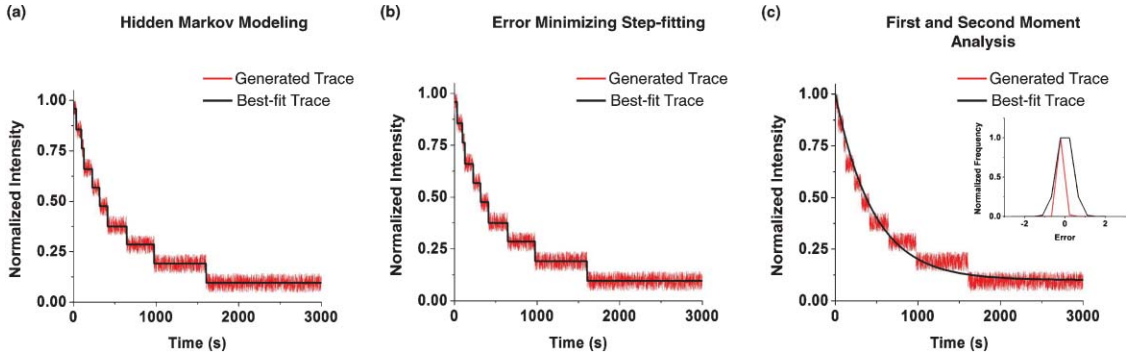

FIG. 6. Comparison of fitting algorithms. Simulated traces were fitted using (a) hidden Markov modeling, (b) error-minimized fitting, and (c) moment analysis, including the first moment (c) and the second moment (c, inset). Fitting simulated traces to idealized, step-like traces using hidden Markov modeling and error-minimized fitting resulted in nearly identical fits. Fits obtained using the moment analysis, on the other hand, resulted in exponential decays characteristic of ensemble measurements in bulk solution.

modeled as a normal distribution with probability density function

$$f(I(t) - \langle I \rangle(t)) = \frac{1}{\sqrt{2\pi\sigma^2}} e^{\frac{-(I(t)-\langle I \rangle(t))^2}{2\sigma^2}} \tag{10}$$

and a standard deviation, σ. Both the first moment $\langle I \rangle$ and second central moment (σ^2) are fit to the simulated data via weighted error minimization.

Typical fits obtained using the three fitting algorithms, the error-minimized step fitting, hidden Markov modeling, and moment analysis, are shown in Figure 6. Although the error-minimization algorithm and hidden Markov model rely on two fundamentally different approaches for fitting traces to the simulated data, they both result in nearly identical fits. Because the hidden Markov model is significantly more computationally time intensive than the error-minimization fits, herein the error-minimization fit will be used in lieu of the fits obtained with the Markov model.

V. STEP 3: CALCULATING FORWARD AND REVERSE RATE CONSTANTS

Forward and reverse rate constants are calculated from the fits once the simulated data are fit to idealized traces. Four methods were used to calculate rate constants: moment analysis, site probability calculations assuming site independence,[33,37] site probability calculations assuming site dependence, and birth-and-death population modeling.[56]

A. Moment analysis

The moment analysis can only calculate rate constants for traces fit using the first and second moments. The rate constants are directly determined from the best-fit first and second moments according to the deterministic relations discussed above.

B. Single-site probability calculations (site independence)

The remaining three methods for calculating rate constants were applied to traces fit using the step-fitting error minimization (see discussion above on comparison of fits to Markov modeling). For the site probability calculations, we assume a Poisson rate process convolution model described in previous studies.[37,57,58] We consider the probability of a site going from an unquenched to a quenched state as P_1 and the probability of a site going from a quenched to an unquenched state as P_2. Therefore, the probability of an unquenched site remaining unquenched is $1-P_1$, and the probability of a quenched site remaining quenched is $1-P_2$. If we consider a nanotube with only 2 indistinguishable binding sites, 3 florescence states are possible: two quenched sites (minimum florescence, state$_1$), two unquenched sites (maximum florescence, state$_3$), and one quenched and one unquenched site (intermediate florescence state, state$_2$). The probability of the nanotube florescence exhibiting a step decrease in florescence from a completely unquenched state for the next timestep is proportional to the product of the probability of one site remaining unquenched, $1-P_1$, and the other site quenching, P_1. These probability expressions can be set equal to the experimental probabilities, which are determined as the number of times the best-fit trace shows a step decrease (or step increase) in florescence divided by the number of 1-s fluorescence measurements, and solved for P_1 and P_2. For the case of a two-site model, the governing equations are

$$P_1(1 - P_1) = \frac{N_{transitions}(state_3 \rightarrow state_2)}{\tau_{dwell}(state_3)}, \tag{11}$$

$$(1 - P_1)^2 = \frac{N_{transitions}(state_3 \rightarrow state_3)}{\tau_{dwell}(state_3)}, \tag{12}$$

$$P_1^2 = \frac{N_{transitions}(state_3 \rightarrow state_1)}{\tau_{dwell}(state_3)}, \tag{13}$$

$$P_2(1 - P_2) = \frac{N_{transitions}(state_1 \rightarrow state_2)}{\tau_{dwell}(state_1)}, \tag{14}$$

$$(1 - P_2)^2 = \frac{N_{transitions}(state_1 \rightarrow state_1)}{\tau_{dwell}(state_1)}, \tag{15}$$

$$P_2^2 = \frac{N_{transitions}(state_1 \rightarrow state_3)}{\tau_{dwell}(state_1)}, \tag{16}$$

$$P_1(1 - P_2) = \frac{N_{transitions}(state_2 \rightarrow state_1)}{\tau_{dwell}(state_2)}, \tag{17}$$

$$P_2(1-P_1) = \frac{N_{transitions}(state_2 \rightarrow state_3)}{\tau_{dwell}(state_2)}, \quad (18)$$

$$(1-P_1)(1-P_2) = \frac{N_{transitions}(state_2 \rightarrow state_2)}{\tau_{dwell}(state_2)}, \quad (19)$$

where $N_{transitions}(state_X \rightarrow state_Y)$ designates the total number of transitions from $state_X$ to $state_Y$, and $\tau_{dwell}(state_X)$ is the total amount of time frames occupied in the initial state $state_X$. In this model, we assume that the probability of a particular site quenching or de-quenching is the same regardless of the state; the site probabilities are treated independently of each other.

C. Single-site probability calculations (site dependence)

An alternative approach to these calculations is to assume that the probability of a particular site quenching or de-quenching is dependent on the state of the sensor, such as the florescence intensity of nanotube sensor. For example, in our two-site nanotube model, the probability of both sites quenching would be half the probability of one site quenching. This approach will change the probability expressions written for each nanotube state, although the resulting probabilities are calculated in an analogous manner (i.e., set expressions equal to the experimental value, solve for the probabilities). Once single-site quenching and de-quenching probabilities have been determined, the corresponding rate constants are calculated using the probability-rate constant expression derived from Gillespie,[51]

$$k_f = \frac{2\ln\left(\frac{1}{1-P_1}\right)}{\Delta t}, \quad (20)$$

$$k_r = \frac{2\ln\left(\frac{1}{1-P_2}\right)}{\Delta t}. \quad (21)$$

D. Birth-and-death population modeling

An alternative to extracting rate constants from idealized, best-fit traces is using the birth-and-death population modeling approach.[35,59] To summarize, in this model, a quenching event is treated as a "death" with rate of k_f, and a de-quenching event is treated as a "birth" with rate of k_r. Based on these analogies, the florescence value of a nanotube at any given time point is equivalent to the total population at that time. So, assuming a nanotube is at a florescence state i at a given time t_0, the probability it will be at state j at time $t + \Delta t$ is dependent on whether the final state j is a de-quenched state ($j = i + 1$), a quenched state ($j = i - 1$), or an unchanged state ($j = i$),

$$P(I_{t_0+\Delta t} = j | I_{t_0} = i) = \begin{cases} (I_{max} - i)k_r \Delta t & \text{if } j = i+1 \\ 1 - (I_{max} - i)k_r \Delta t - i k_f \Delta t & \text{if } j = i \\ i k_f \Delta t & \text{if } j = i-1 \end{cases}, \quad (22)$$

where I_{max} is the maximum intensity state. Mathematically, Eq. (22) represents a Markov jump process, allowing the likelihood, L, of the observed process to be expressed as[35,56]

$$L = \prod_{i=1}^{n(t)} P(I_{t_0+\Delta t} = j | I_{t_0} = i) e^{-\int_0^t T(X_u) du}, \quad (23)$$

where $n(t)$ is the number of jumps at time t and $T(X_u)$ is defined as

$$T(X_u) = (I_{max} - I_u)k_r + I_u k_f. \quad (24)$$

Now we define g, the probabilities of transitioning to state j from state i for the next transition, and S_t, the total time lived by a population during the trace time interval $[0, t]$,

$$g(I_{t_0+\Delta t} = j | I_{t_0} = i) = \begin{cases} N_{quenched} k_r & \text{if } j = i+1 \\ i k_f & \text{if } j = i-1 \\ 0 & \text{otherwise} \end{cases}, \quad (25)$$

$$S_t = \int_0^t I_u du. \quad (26)$$

This gives

$$L = \prod_{i=1}^{n(t)} g(I_{t_0+\Delta t} = j | I_{t_0} = i) e^{(I_{max} k_r t + (k_f - k_r) S_t)}. \quad (27)$$

The maximum likelihood estimators of k_f and k_r are found by maximizing the above probability expression. To convert the product to a summation, it is most convenient to take the derivatives of the natural log of Eq. (27), which leads to the following estimators:[35]

$$k_f = \frac{N_{quenched}}{S_t}, \quad (28)$$

$$k_r = \frac{N_{de\text{-}quenched}}{I_{max} t - S_t}. \quad (29)$$

where $N_{quenched}$ is the number of instances the trace undergoes a quenching step, $N_{de\text{-}quenched}$ is the number of instances the trace undergoes a de-quenching step, and t is the total time of the trace.

VI. COMPARING RELATIVE ERROR AMONG THE DIFFERENT ALGORITHMS

The forward and reverse rate constants calculated using each of the algorithms described above were compared to the actual rate constants that were initially used to generate the KMC traces. The relative error, ε_{rel}, was calculated between the actual (k_{input}) and calculated ($k_{calculated}$) forward rate constants and normalized with respect to the actual value, or

$$\varepsilon_{rel} = \frac{|k_{input} - k_{calculated}|}{k_{input}}. \quad (30)$$

This error was averaged over the 100 traces simulated at a particular forward rate, reverse rate, and noise level. A summary of this mean error for different rate and noise conditions is shown in Figure 7. Overall, the single-site probability approaches to calculating rate constants demonstrated the

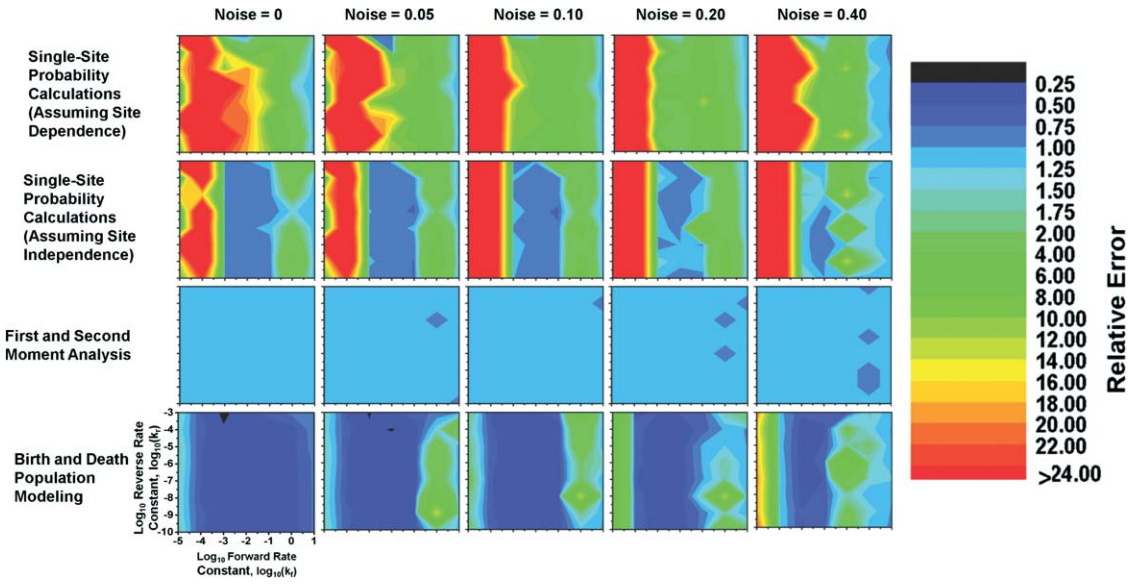

FIG. 7. Comparison of relative error for various k_f and k_r values. Relative error between calculated and actual forward rate constants were calculated when varying actual forward and reverse rate constants. Error plots were generated using 4 different algorithms (single-site probability calculations assuming dependent quenching rate constants, single-site probability calculations assuming independent quenching rate constants, first and second moment analysis, and birth-and-death modeling) at 5 different noise levels. Overall, relative error increases with increasing noise levels, with some algorithms, such as the moment analysis, less affected by the noise level. For rate constants on the order of those demonstrated in literature ($k_f \sim 10^{-3}$ s^{-1}, $k_r \sim 10^{-7}$ s^{-1}), the birth-and-death population modeling exhibits the least relative error.

largest amount of error; the moment analysis and birth-and-death population modeling resulted in the least amount of error. Under typical experimental conditions, with $k_f \sim 10^{-3}$ s^{-1} and $k_r \sim 10^{-7}$ s^{-1}, the birth-and-death model provides the least amount of error. For each plot, the largest amount of error tends to occur at the highest and lowest values of k_f.

For all the algorithms, overall error increases with increasing noise levels. However, these algorithms exhibited varying sensitivities to noise. The first and second moment analysis demonstrates the least sensitivity toward noise level. This is due to the deterministic nature of this approach. Specifically, this algorithm fits the traces to the deterministic equation for ensemble measurement, which for first order adsorption is an exponential decay with time. Although increased noise levels may mask the existence of a step in a trace, the moment analysis does not rely on the existence of step-like changes in florescence over time; instead it relies on the overall decaying trend of the trace, which remains largely unaffected by noise.

On the other hand, the error calculated from algorithms that rely on step-like changes in intensity over time was significantly affected by noise. As shown in Figure 8, as

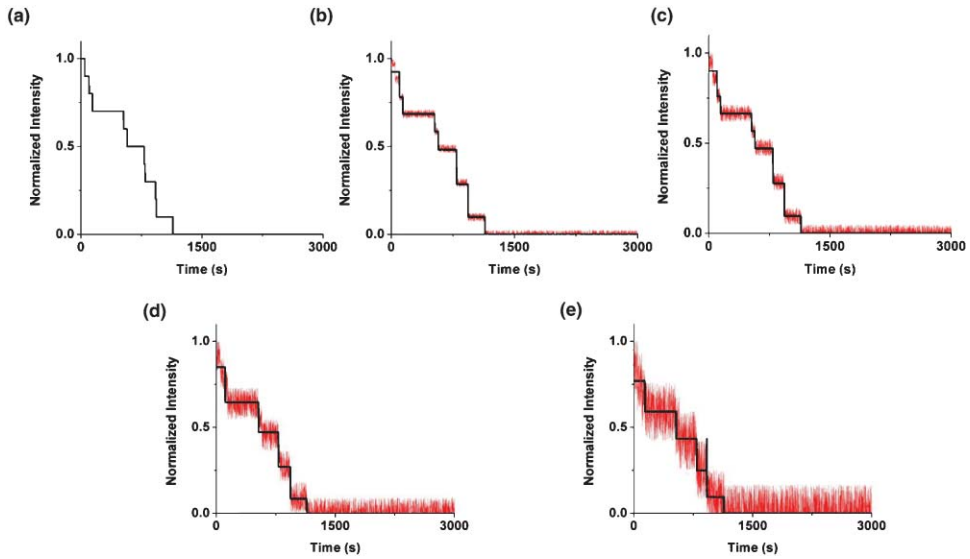

FIG. 8. Effect of noise on fitting traces. Error-minimized fits were obtained for traces with noise levels of (a) 0, (b) 0.05, (c) 0.10, (d) 0.20, and (e) 0.40, with sample traces and fits as shown. Increased noise levels results in both the erroneous fitting of nonexistent transitions and the omission of existent transitions. These discrepancies result in the increased error in the calculated rate constants.

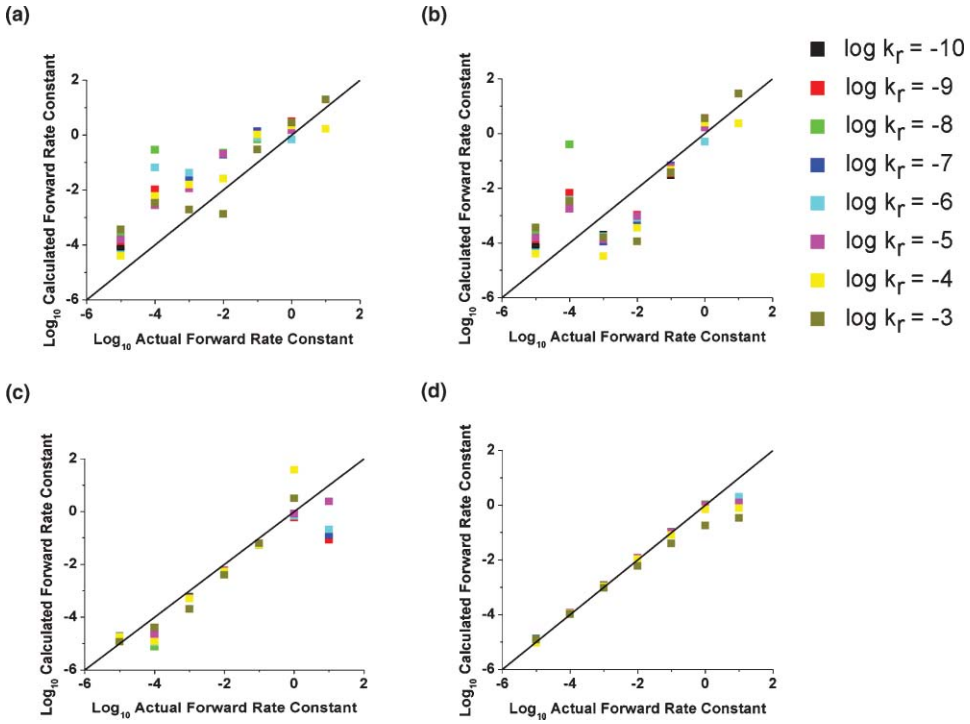

FIG. 9. Comparison of actual and calculated rate constants. Actual and calculated rate constants were compared for (a) single-site probability calculations assuming dependent quenching rate constants, (b) single-site probability calculations assuming independent quenching rate constants, (c) first and second moment analysis, and (d) birth-and-death modeling. For comparison, a trendline with a slope of 1 was included to demonstrate ideal behavior of an algorithm where calculated rate constant is precisely equal to the actual rate constant.

noise level increases, the error-minimization fitting algorithm largely neglects to fit steps that are masked by the decreased signal-to-noise ratio while occasionally introducing fictitious states demonstrated by the noise. Hence, the increase in error at high noise levels is due to the failure of the step-fitting algorithms used in the second step of this analysis.

In addition to examining relative error, we also directly compared the calculated rate constant with the actual constant at different reverse rates (Figure 9). All algorithms tested were able to calculate an increased rate constant for traces simulated at higher rates. When compared to the idealized trendline where calculated rate is precisely equal to the actual rate (slope = 1), the algorithms demonstrate varying degrees of conformity, with the birth-and-death modeling algorithm demonstrating the highest degree of conformity. At large values of k_f, the algorithm begins to underestimate rate constants. At these values, the traces exhibit complete quenching within the first few seconds of the simulation, where it becomes more difficult to distinguish very high rates from even higher rates.

VII. CONCLUSION

A comparison of the various algorithms used to calculate rate constants from single-molecule intensity traces reveals that precision is dependent not only on the algorithm used, but also the noise level of the data and the magnitude of the forward and reverse rates. Greatest error was observed at extreme values of k_f (very large and very small forward rate constants) and at small signal-to-noise ratios. The algorithms exhibited varying degrees of sensitivity to noise, with the first and second moment analysis being the least sensitive. Overall, forward rate constants were recovered most accurately using the birth-and-death population model, mostly in the regimes most relevant to the experimental conditions.

ACKNOWLEDGMENTS

The authors are grateful for the intellectual discussions with Andrew J. Hilmer regarding the Monte Carlo simulation. The authors are also grateful for funding from the Beckman Foundation, the National Science Foundation, and the DuPont-MIT Alliance. A.A.B is grateful for support from the National Defense Science and Engineering Graduate Fellowship, Z.W.U. is grateful for support from the Department of Energy Fellowship, and N.F.R. is grateful for support from the National Science Foundation Fellowship.

[1]S. Weiss, Science **283**(5408), 1676 (1999).
[2]T. J. Ha, A. Y. Ting, J. Liang, W. B. Caldwell, A. A. Deniz, D. S. Chemla, P. G. Schultz, and S. Weiss, Proc. Natl. Acad. Sci. U.S.A. **96**(3), 893 (1999).
[3]A. A. Deniz, M. Dahan, J. R. Grunwell, T. J. Ha, A. E. Faulhaber, D. S. Chemla, S. Weiss, and P. G. Schultz, Proc. Natl. Acad. Sci. U.S.A. **96**(7), 3670 (1999).
[4]T. Ha, T. A. Laurence, D. S. Chemla, and S. Weiss, J. Phys. Chem. B **103**(33), 6839 (1999).
[5]X. H. Xu and E. S. Yeung, Science **275**(5303), 1106 (1997).
[6]D. Y. Chen and N. J. Dovichi, Anal. Chem. **68**(4), 690 (1996).
[7]E. Geva and J. L. Skinner, Chem. Phys. Lett. **288**(2–4), 225 (1998).
[8]B. J. Davis, A. K. Swan, M. S. Unlu, W. C. Karl, B. B. Goldberg, J. C. Schotland, and P. S. Carney, J. Opt. Soc. Am. A Opt. Image Sci. Vis. **24**(11), 3587 (2007).

[9]T. Funatsu, Y. Harada, M. Tokunaga, K. Saito, and T. Yanagida, Nature (London) **374**(6522), 555 (1995).
[10]J. Eid, A. Fehr, J. Gray, K. Luong, J. Lyle, G. Otto, P. Peluso, D. Rank, P. Baybayan, B. Bettman, A. Bibillo, K. Bjornson, B. Chaudhuri, F. Christians, R. Cicero, S. Clark, R. Dalal, A. Dewinter, J. Dixon, M. Foquet, A. Gaertner, P. Hardenbol, C. Heiner, K. Hester, D. Holden, G. Kearns, X. X. Kong, R. Kuse, Y. Lacroix, S. Lin, P. Lundquist, C. C. Ma, P. Marks, M. Maxham, D. Murphy, I. Park, T. Pham, M. Phillips, J. Roy, R. Sebra, G. Shen, J. Sorenson, A. Tomaney, K. Travers, M. Trulson, J. Vieceli, J. Wegener, D. Wu, A. Yang, D. Zaccarin, P. Zhao, F. Zhong, J. Korlach, and S. Turner, Science **323**(5910), 133 (2009).
[11]G. Peleg, P. Ghanouni, B. K. Kobilka, and R. N. Zare, Proc. Natl. Acad. Sci. U.S.A. **98**(15), 8469 (2001).
[12]L. P. Watkins and H. Yang, Biophys. J. **86**(6), 4015 (2004).
[13]O. Krichevsky and G. Bonnet, Rep. Prog. Phys. **65**(2), 251 (2002).
[14]T. E. Turner, S. Schnell, and K. Burrage, Comput. Biol. Chem. **28**(3), 165 (2004).
[15]H. P. Lu, L. Y. Xun, and X. S. Xie, Science **282**(5395), 1877 (1998).
[16]K. A. Henzler-Wildman, V. Thai, M. Lei, M. Ott, M. Wolf-Watz, T. Fenn, E. Pozharski, M. A. Wilson, G. A. Petsko, M. Karplus, C. G. Hubner, and D. Kern, Nature (London) **450**(7171), 838 (2007).
[17]X. W. Zhuang, H. Kim, M. J. B. Pereira, H. P. Babcock, N. G. Walter, and S. Chu, Science **296**(5572), 1473 (2002).
[18]B. P. English, W. Min, A. M. van Oijen, K. T. Lee, G. B. Luo, H. Y. Sun, B. J. Cherayil, S. C. Kou, and X. S. Xie, Nat. Chem. Biol. **2**(2), 87 (2006).
[19]A. Miyawaki, J. Llopis, R. Heim, J. M. McCaffery, J. A. Adams, M. Ikura, and R. Y. Tsien, Nature (London) **388**(6645), 882 (1997).
[20]B. Schuler, E. A. Lipman, and W. A. Eaton, Nature (London) **419**(6908), 743 (2002).
[21]Y. W. Jia, D. S. Talaga, W. L. Lau, H. S. M. Lu, W. F. DeGrado, and R. M. Hochstrasser, Chem. Phys. **247**(1), 69 (1999).
[22]A. A. Deniz, T. A. Laurence, G. S. Beligere, M. Dahan, A. B. Martin, D. S. Chemla, P. E. Dawson, P. G. Schultz, and S. Weiss, Proc. Natl. Acad. Sci. U.S.A. **97**(10), 5179 (2000).
[23]S. Weiss, Nat. Struct. Biol. **7**(9), 724 (2000).
[24]D. S. Talaga, W. L. Lau, H. Roder, J. Y. Tang, Y. W. Jia, W. F. DeGrado, and R. M. Hochstrasser, Proc. Natl. Acad. Sci. U.S.A. **97**(24), 13021 (2000).
[25]L. Romberg, D. W. Pierce, and R. D. Vale, J. Cell Biol. **140**(6), 1407 (1998).
[26]Y. Suzuki, T. Yasunaga, R. Ohkura, T. Wakabayashi, and K. Sutoh, Nature (London) **396**(6709), 380 (1998).
[27]A. N. Kapanidis, N. K. Lee, T. A. Laurence, S. Doose, E. Margeat, and S. Weiss, Proc. Natl. Acad. Sci. U.S.A. **101**(24), 8936 (2004).
[28]R. Rigler, A. Pramanik, P. Jonasson, G. Kratz, O. T. Jansson, P. A. Nygren, S. Stahl, K. Ekberg, B. L. Johansson, S. Uhlen, M. Uhlen, H. Jornvall, and J. Wahren, Proc. Natl. Acad. Sci. U.S.A. **96**(23), 13318 (1999).
[29]E. Haustein and P. Schwille, Methods **29**(2), 153 (2003).
[30]K. Bacia and P. Schwille, Methods **29**(1), 74 (2003).
[31]L. A. Neely, S. Patel, J. Garver, M. Gallo, M. Hackett, S. McLaughlin, M. Nadel, J. Harris, S. Gullans, and J. Rooke, Nat. Methods **3**(1), 41 (2006).
[32]M. C. Leake, J. H. Chandler, G. H. Wadhams, F. Bai, R. M. Berry, and J. P. Armitage, Nature (London) **443**(7109), 355 (2006).
[33]H. Jin, D. A. Heller, M. Kalbacova, J. H. Kim, J. Q. Zhang, A. A. Boghossian, N. Maheshri, and M. S. Strano, Nat. Nanotechnol. **5**(4), 302 (2010).
[34]L. Cognet, D. A. Tsyboulski, J. D. R. Rocha, C. D. Doyle, J. M. Tour, and R. B. Weisman, Science **316**(5830), 1465 (2007).
[35]J. Q. Zhang, A. A. Boghossian, P. W. Barone, A. Rwei, J. H. Kim, D. Lin, D. A. Heller, A. J. Hilmer, N. Nair, N. F. Reuel, and M. S. Strano, J. Am. Chem. Soc. **133**(3), 567 (2011).
[36]D. A. Heller, H. Jin, B. M. Martinez, D. Patel, B. M. Miller, T. K. Yeung, P. V. Jena, C. Hobartner, T. Ha, S. K. Silverman, and M. S. Strano, Nat. Nanotechnol. **4**(2), 114 (2009).
[37]H. Jin, D. A. Heller, J. H. Kim, and M. S. Strano, Nano Lett. **8**(12), 4299 (2008).
[38]D. S. Talaga, Curr. Opin. Colloid Interface Sci. **12**(6), 285 (2007).
[39]M. Andrec, R. M. Levy, and D. S. Talaga, J. Phys. Chem. A **107**(38), 7454 (2003).
[40]M. Jager, A. Kiel, D. P. Herten, and F. A. Hamprecht, ChemPhysChem **10**(14), 2486 (2009).
[41]G. F. Schroder and H. Grubmuller, J. Chem. Phys. **119**(18), 9920 (2003).
[42]H. Yang, G. B. Luo, P. Karnchanaphanurach, T. M. Louie, I. Rech, S. Cova, L. Y. Xun, and X. S. Xie, Science **302**(5643), 262 (2003).
[43]T. C. Messina, H. Y. Kim, J. T. Giurleo, and D. S. Talaga, J. Phys. Chem. B **110**(33), 16366 (2006).
[44]S. A. McKinney, C. Joo, and T. Ha, Biophys. J. **91**(5), 1941 (2006).
[45]C. Joo, S. A. McKinney, M. Nakamura, I. Rasnik, S. Myong, and T. Ha, Cell **126**(3), 515 (2006).
[46]D. S. Talaga, J. Phys. Chem. A **110**(31), 9743 (2006).
[47]D. S. Talaga, J. Phys. Chem. A **113**(17), 5251 (2009).
[48]A. F. Voter, in *Radiation Effects in Solids*, edited by E. A. K. Kurt, E. Sickafus, and Blas P. Uberuaga (Springer, NATO Publishing Unit, Dordrecht, 2005).
[49]D. M. Harrah and A. K. Swan, ACS Nano **5**(1), 647 (2010).
[50]D. T. Gillespie, Annu. Rev. Phys. Chem. **58**, 35 (2007).
[51]D. T. Gillespie, J. Phys. Chem. **81**(25), 2340 (1977).
[52]Z. W. Ulissi, J. Q. Zhang, A. A. Boghossian, N. F. Reuel, S. F. E. Shimizu, R. D. Braatz, and M. S. Strano, J. Phys. Chem. Lett. **2**, 1690 (2011).
[53]J. W. J. Kerssemakers, E. L. Munteanu, L. Laan, T. L. Noetzel, M. E. Janson, and M. Dogterom, Nature (London) **442**(7103), 709 (2006).
[54]S. R. Eddy, Nat. Biotechnol. **22**(10), 1315 (2004).
[55]T. Jahnke and W. Huisinga, J. Math. Biol. **54**(1), 1 (2007).
[56]P. D. Feigin, Adv. Appl. Probab. **8**(4), 712 (1976).
[57]Y. M. Wang and H. P. Lu, J. Phys. Chem. B **114**(19), 6669 (2010).
[58]H. P. Lu, Phys. Chem. Chem. Phys. **13**(15), 6734 (2011).
[59]N. Keiding, Ann. Stat. **3**(2), 363 (1975).